Competition between Al_2O_3 atomic layer etching and AlF_3 atomic layer deposition using sequential exposures of trimethylaluminum and hydrogen fluoride

Jaime W. DuMont[1] and Steven M. George[1,2]
[1]*Department of Chemistry and Biochemistry, University of Colorado, Boulder, Colorado 80309-0215, USA*
[2]*Department of Mechanical Engineering, University of Colorado, Boulder, Colorado 80309-0215, USA*

(Received 20 August 2016; accepted 8 December 2016; published online 4 January 2017)

The thermal atomic layer etching (ALE) of Al_2O_3 can be performed using sequential and self-limiting reactions with trimethylaluminum (TMA) and hydrogen fluoride (HF) as the reactants. The atomic layer deposition (ALD) of AlF_3 can also be accomplished using the same reactants. This paper examined the competition between Al_2O_3 ALE and AlF_3 ALD using *in situ* Fourier transform infrared (FTIR) vibrational spectroscopy measurements on Al_2O_3 ALD-coated SiO_2 nanoparticles. The FTIR spectra could observe an absorbance loss of the Al-O stretching vibrations during Al_2O_3 ALE or an absorbance gain of the Al-F stretching vibrations during AlF_3 ALD. The transition from AlF_3 ALD to Al_2O_3 ALE occurred versus reaction temperature and was also influenced by the N_2 or He background gas pressure. Higher temperatures and lower background gas pressures led to Al_2O_3 ALE. Lower temperatures and higher background gas pressures led to AlF_3 ALD. The FTIR measurements also monitored $AlCH_3^*$ and HF^* species on the surface after the TMA and HF reactant exposures. The loss of $AlCH_3^*$ and HF^* species at higher temperatures is believed to play a vital role in the transition between AlF_3 ALD at lower temperatures and Al_2O_3 ALE at higher temperatures. The change between AlF_3 ALD and Al_2O_3 ALE was defined by the transition temperature. Higher transition temperatures were observed using larger N_2 or He background gas pressures. This correlation was associated with variations in the N_2 or He gas thermal conductivity versus pressure. The fluorination reaction during Al_2O_3 ALE is very exothermic and leads to temperature rises in the SiO_2 nanoparticles. These temperature transients influence the Al_2O_3 etching. The higher N_2 and He gas thermal conductivities are able to cool the SiO_2 nanoparticles more efficiently and minimize the size of the temperature rises. The competition between Al_2O_3 ALE and AlF_3 ALD using TMA and HF illustrates the interplay between etching and growth and the importance of substrate temperature. Background gas pressure also plays a key role in determining the transition temperature for nanoparticle substrates. *Published by AIP Publishing.* [http://dx.doi.org/10.1063/1.4973310]

I. INTRODUCTION

Atomic layer processes such as atomic layer deposition (ALD) and atomic layer etching (ALE) are techniques that can add or remove material with atomic level precision using sequential, self-limiting surface reactions.[1,2] Deposition and removal processes at the atomic scale are crucial for the engineering and fabrication of semiconductor devices.[3] Many thermal chemistries and processes have been developed for ALD.[4] In contrast, thermal processes have been developed only recently for ALE.[5–10]

The recently developed thermal ALE processes are based on sequential fluorination and ligand-exchange reactions.[5,9,11] Fluorination converts the metal compound, such as a metal oxide, to a metal fluoride. A metal precursor then undergoes a ligand-exchange transmetalation reaction. During ligand-exchange, the metal precursor accepts fluorine from the metal fluoride and donates one of its ligands to the surface and produces volatile reaction products that lead to etching.[5,9,11]

HF has been a successful fluorine precursor for Al_2O_3, HfO_2, AlF_3, and AlN ALE.[5–10] HF is also an effective fluorine precursor for the ALD of a variety of metal fluoridess such as AlF_3, ZrF_4, HfF_4, MnF_2, MgF_2, ZnF_2, and LiF.[12] Trimethylaluminum (TMA) is the most common precursor for Al_2O_3 ALD and AlF_3 ALD.[13,14] TMA can also serve as a metal precursor for Al_2O_3 ALE.[8] The ability of the TMA and HF precursors to produce either Al_2O_3 ALE or AlF_3 ALD indicates that there is competition between the etching and growth processes.

For AlF_3 ALD using TMA and HF, TMA and HF react to produce AlF_3 according to $Al(CH_3)_3 + 3HF \rightarrow AlF_3 + 3CH_4$.[14] Figure 1(a) shows a schematic of AlF_3 ALD on an Al_2O_3 substrate at low temperatures. In the sequential, self-limiting surface reactions, TMA reacts with HF species on the surface to form $AlF_x(CH_3)_{3-x}^*$ surface intermediates. HF then fluorinates these surface intermediates to form AlF_3 and additional HF^* species on the surface.[14] The temperature dependence of the AlF_3 ALD growth rate is believed to be related to the stability of the $AlF_x(CH_3)_{3-x}^*$ and HF^* surface species.

At higher temperatures, the $AlF_x(CH_3)_{3-x}^*$ and HF^* surface intermediates may overcome their binding energies and desorb from the surface. As a result, HF can then act to fluorinate the underlying Al_2O_3 substrate to form an AlF_3 layer

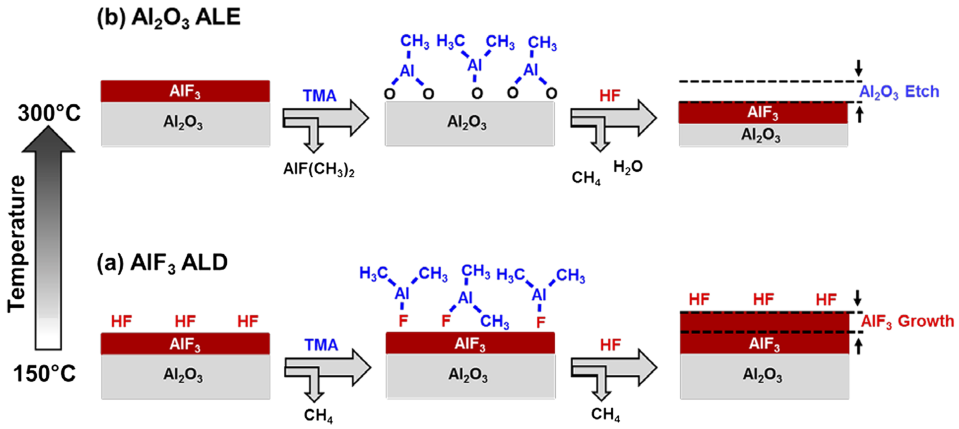

FIG. 1. Schematic for (a) AlF_3 ALD at a low temperature of 150 °C and (b) Al_2O_3 ALE at a high temperature of 300 °C. Both AlF_3 ALD and Al_2O_3 ALE utilize TMA and HF as the reactants.

according to $Al_2O_3 + 6HF \rightarrow 2AlF_3 + 3H_2O$.[5,9,11] During the TMA exposures, TMA then accepts fluorine from the newly formed AlF_3 layer in a ligand-exchange process.[8] TMA also donates CH_3 ligands to the surface to form volatile $AlF(CH_3)_2$ species. The desorption of these species results in an overall loss of the original Al_2O_3 film. Additional $AlCH_3^*$ species may also be formed by TMA adsorption on the Al_2O_3 substrate after the removal of the AlF_3 layer.[8] A schematic of Al_2O_3 ALE at higher temperatures is displayed in Figure 1(b).

In this paper, sequential exposures of TMA and HF were employed for thermal Al_2O_3 ALE and thermal AlF_3 ALD. *In situ* Fourier transform infrared (FTIR) measurements were used to study the rivalry between these etching and growth processes. The infrared spectra were used to observe the absorbance loss of the Al–O stretching vibrations or the absorbance gain of the Al–F stretching vibrations. These FTIR measurements could also monitor the surface species during each reactant exposure. These studies reveal that the surface temperature and the thermal stability of the surface intermediates lead to either Al_2O_3 ALE or AlF_3 ALD.

II. EXPERIMENTAL

The surface chemistry during sequential exposures of TMA and HF on Al_2O_3 films at various reaction temperatures was studied using *in situ* FTIR spectroscopy. The *in situ* FTIR studies were performed in a reactor equipped with an FTIR spectrometer that has been described previously.[15] The FTIR experiments utilized high surface area SiO_2 nanoparticles (99.5%, US Research Nanomaterials) with an average diameter of 15–20 nm. The large surface area provided by the nanopowder substrates improved the signal-to-noise ratio for infrared absorption. The SiO_2 nanoparticles absorb infrared radiation between 400 and 650 cm^{-1}, 700 and 875 cm^{-1}, and 925 and 1400 cm^{-1}. In between these absorbance regions are open windows at 650–700 cm^{-1} and 875–925 cm^{-1} to monitor absorbance changes from the species during both AlF_3 ALD and Al_2O_3 ALE.

The SiO_2 nanoparticles were mechanically pressed into a tungsten grid support to obtain transmission FTIR measurements.[16,17] The sample grids were 2 cm × 3 cm in size and 50 μm thick, and contained 100 grid lines per inch. The tungsten grid could be resistively heated using a DC power supply (6268B, 20 V/20 A, Hewlett-Packard). The voltage output of the power supply was controlled by a proportional–integral–derivative (PID) temperature controller (Love Controls 16B, Dwyer Instruments). A type K thermocouple was secured to the bottom of the tungsten grid with epoxy (Ceramabond 571, Aremco) that attached and electrically isolated the thermocouple.

The Al_2O_3 films were grown on the SiO_2 nanoparticles with Al_2O_3 ALD using TMA (97%, Sigma-Aldrich) and H_2O (Chromasolv for HPLC, Sigma-Aldrich) at 170 °C. The TMA exposures were ~1.00 Torr s and the H_2O exposures were ~0.75 Torr s. Each exposure was separated by a 180 s purge to remove excess reactant and reaction byproducts from the chamber. A constant flow of 100 sccm of ultra-high purity (UHP) N_2 gas was delivered into the reactor during the Al_2O_3 ALD reactions. The total N_2 gas flow resulted in a base pressure of ~1 Torr that was continuously pumped by a mechanical pump.

The Al_2O_3 ALD layers grown on the SiO_2 nanoparticles were subsequently subjected to alternating exposures of TMA (97%, Sigma-Aldrich) and HF derived from HF-pyridine (70 wt. % HF, Sigma-Aldrich) at various reaction temperatures. Both the TMA and HF exposures were ~1.00 Torr s with each exposure separated by a 240 s purge. In addition to changing the reaction temperature, the flow of carrier gas as well as the carrier gas itself was varied to study the effect of pressure and carrier gas on the AlF_3 ALD and Al_2O_3 ALE and the transition temperature between AlF_3 ALD and Al_2O_3 ALE.

III. RESULTS AND DISCUSSION

A. Competition between AlF_3 ALD and Al_2O_3 ALE

The surface reactions of TMA and HF on Al_2O_3 ALD-coated SiO_2 nanoparticles were studied by *in situ* transmission FTIR spectroscopy. After the nanoparticles were coated with 10 Al_2O_3 ALD cycles using TMA and H_2O as the reactants, the sample was sequentially exposed to TMA and HF at 15 °C intervals between 155 and 245 °C. Figure 2 shows the change in absorbance between 500 and 1200 cm^{-1} after 1, 5, and 10 TMA/HF cycles on an Al_2O_3 ALD film at various reaction temperatures. The spectra are referenced to the Al_2O_3 ALD-

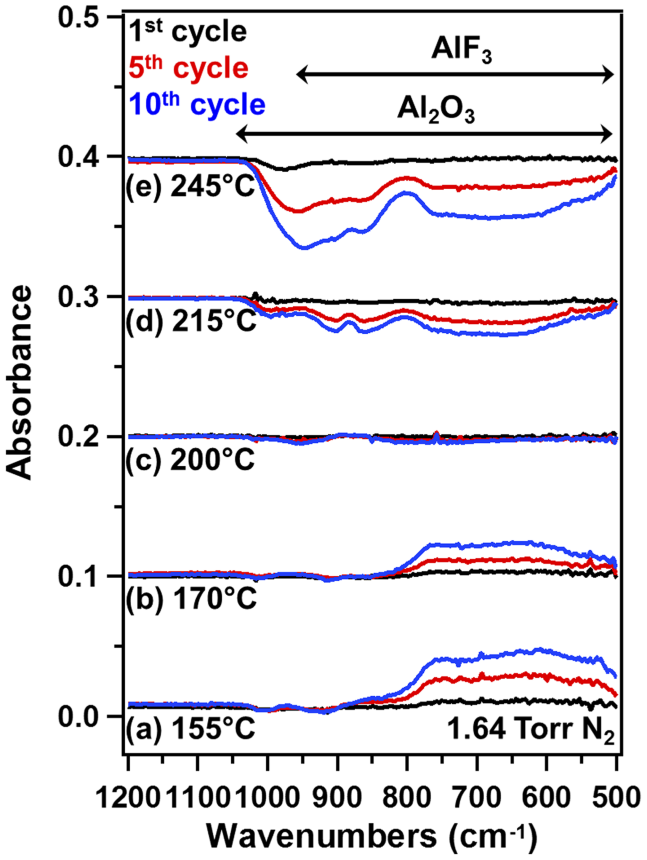

FIG. 2. Absorbance spectra showing the growth of Al–F stretching vibrations in AlF_3 or the removal of Al–O stretching vibrations in Al_2O_3 versus 1, 5, and 10 TMA/HF cycles at (a) 155, (b) 170, (c) 200, (d) 215, and (e) 245 °C. These spectra were recorded with an N_2 base pressure of 1.64 Torr after HF exposures and were referenced to the initial Al_2O_3 ALD-coated SiO_2 nanoparticles.

coated SiO_2 nanoparticle substrate and are displaced from the origin for clarity in presentation. The experiments were run under a constant flow of 150 sccm of UHP N_2 that resulted in a N_2 background pressure of 1.64 Torr in the reactor.

At 155 °C in Figure 2(a), an absorbance gain is observed between 500 and 900 cm^{-1} that is attributed to the Al–F stretching vibrations in AlF_3.[18,19] This absorbance gain is consistent with AlF_3 ALD. Previous studies of AlF_3 ALD have shown that sequential exposures of TMA and HF between 75 and 200 °C result in the growth of amorphous AlF_3 films.[14] The reactions during AlF_3 ALD at low temperatures are illustrated in Figure 1(a).

As the reaction temperature is increased to 170 °C, Figure 2(b) reveals that the absorbance gain decreases between 500 and 900 cm^{-1}. This behavior is consistent with the reduced growth rates that were observed for AlF_3 ALD at higher reaction temperatures.[14] As the reaction temperature is increased further to 185 °C (not shown), the absorbance change between 500 and 900 cm^{-1} approaches zero. The absorbance change between 500 and 900 cm^{-1} is nearly unchanged at 200 °C in Figure 2(c). The negligible absorbance reveals the lack of either AlF_3 growth or Al_2O_3 etching.

By 215 °C, Figure 2(d) shows that the absorbance change with TMA/HF reaction cycles displays a progressive absorbance loss between 500 and 1050 cm^{-1}. This decrease is attributed to the loss of absorbance from Al–O stretching vibrations in the underlying Al_2O_3 ALD film. The absorbance of the Al–O stretching vibrations in amorphous Al_2O_3 is broad and ranges from ~550 to 1030 cm^{-1}.[17] This absorbance loss is consistent with Al_2O_3 etching. At 245 °C, Figure 2(e) reveals that the absorbance loss becomes more significant and indicates that higher temperatures result in higher Al_2O_3 etch rates. The Al_2O_3 ALE process was recently reported and is believed to follow the reaction: $Al_2O_3 + 4Al(CH_3)_3 + 6HF \rightarrow 6AlF(CH_3)_2 + 3H_2O$.[8] The reactions during Al_2O_3 ALE at high temperatures are depicted in Figure 1(b).

B. Temperature dependence of surface species

FTIR difference spectra can reveal the changes in surface coverage with each HF and TMA exposure. Figure 3 shows the FTIR difference spectra between 2500 and 4000 cm^{-1} for two consecutive HF and TMA exposures at 170, 200, and 245 °C. These temperatures correspond with AlF_3 ALD, no net growth or etching, and Al_2O_3 ALE, respectively. Each difference spectrum is referenced to the spectrum prior to the exposure. These spectra are displaced from the origin for clarity in presentation.

Figure 3(a) shows the difference spectrum after an HF exposure at 170 °C where AlF_3 ALD occurs. The positive absorbance feature observed between ~3000 and 3675 cm^{-1} is attributed to the gain of absorbance for the stretching vibrations of isolated and hydrogen-bonded HF^* surface species, respectively.[20] The shading highlights this absorbance feature for HF^* surface species. The negative features observed between 2800 and 3000 cm^{-1} correspond to the loss of absorbance from the asymmetric and symmetric stretching vibrations of $AlCH_3^*$ surface species, respectively.[21] The $AlCH_3^*$ surface species include $AlF(CH_3)_2^*$ and $AlF_2(CH_3)^*$ species or

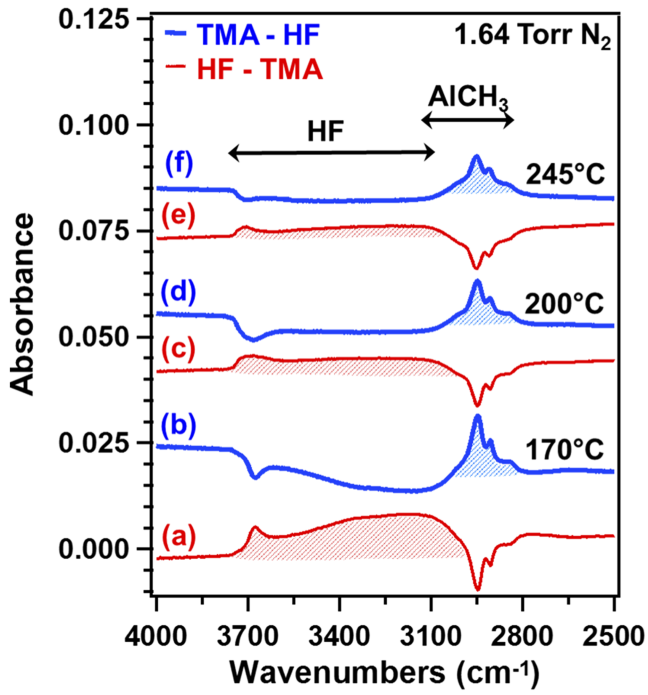

FIG. 3. Difference absorbance spectra from 2500 to 4000 cm^{-1} during TMA/HF exposures at 170, 200, and 245 °C. The difference spectra were recorded after (a), (c), and (e) HF and (b), (d), and (f) TMA exposures and were referenced using the spectra after the previous TMA and HF exposures.

$AlCH_3^*$ species on the Al_2O_3 surface. These species are collectively designated as the $AlCH_3^*$ species. $AlCH_3^*$ species on the Al_2O_3 surface can result from TMA adsorption on Al_2O_3 after removal of the AlF_3 layer.[8]

The infrared difference spectrum after a TMA exposure at 170 °C is shown in Figure 3(b). The loss of absorbance from the HF stretching vibrations indicates that the TMA exposure removes all of the HF^* surface species that were added during the previous HF exposure. The addition of absorbance for vibrational features between 2800 and 3000 cm^{-1} indicates that the TMA exposure replenishes the $AlCH_3^*$ species that were removed during the previous HF exposure. The shading highlights this absorbance feature for the $AlCH_3^*$ species.

Figures 3(c)–3(f) show the difference spectra after two consecutive HF and TMA exposures at 200 and 245 °C, respectively. As the reaction temperature is increased from 170 °C where AlF_3 ALD occurs, the change of absorbance attributed to the HF^* surface species decreases significantly. A ~70% percent reduction in the change of absorbance for the HF^* species is observed as the reaction temperature is increased from 170 to 245 °C where Al_2O_3 ALE occurs. The change of absorbance for the $AlCH_3^*$ species also decreases. An overall ~37% reduction in the change of absorbance for the $AlCH_3^*$ species is observed as the reaction temperature is increased from 170 to 245 °C where Al_2O_3 ALE occurs.

Additional experiments revealed that the HF exposures were able to remove all the $AlCH_3^*$ species and reform all the HF^* species at all temperatures. The TMA exposures were also able to remove all the HF^* species and reform all the $AlCH_3^*$ species at all temperatures. Consequently, the integrated absorbance of the absorbance features for the difference spectra in Figure 3 can be employed to monitor the temperature stability of the $AlCH_3^*$ and HF^* species during the TMA and HF exposures.

Figure 4 displays the normalized integrated absorbance of the $AlCH_3^*$ and HF^* features from the difference spectra between 155 °C and 245 °C. The normalized integrated absorbance for the $AlCH_3^*$ species decreases ~43% between 155 °C and 245 °C. The normalized integrated absorbance for the HF^* species decreases ~84% between 155 °C and 245 °C. The stability of the $AlCH_3^*$ and HF^* species is believed to play an important role in determining the competition between AlF_3 ALD and Al_2O_3 ALE.

At temperatures <200 °C, HF molecules adsorb on the surface after the HF exposure. During the next TMA exposure, TMA can then react with adsorbed HF molecules to form $AlF(CH_3)_2^*$ and $AlF_2(CH_3)^*$ surface species. These $AlF(CH_3)_2^*$ and $AlF_2(CH_3)^*$ species remain on the surface and can be converted to AlF_3 during the next HF exposure. These sequential surface reactions at lower temperatures lead to AlF_3 ALD as illustrated in Figure 1(a).

As the reaction temperature is increased to >200 °C, fewer HF^* surface species remain adsorbed after the HF exposure. However, the HF molecules may be able to fluorinate the Al_2O_3 surface and form an AlF_3 layer according to $Al_2O_3 + 6HF \rightarrow 2AlF_3 + 3H_2O$.[5,9,11] The next TMA exposure does not encounter many HF^* species on the surface. Instead, the TMA can accept fluorine from the AlF_3 layer in a ligand-exchange reaction.[8] This ligand-exchange can form volatile

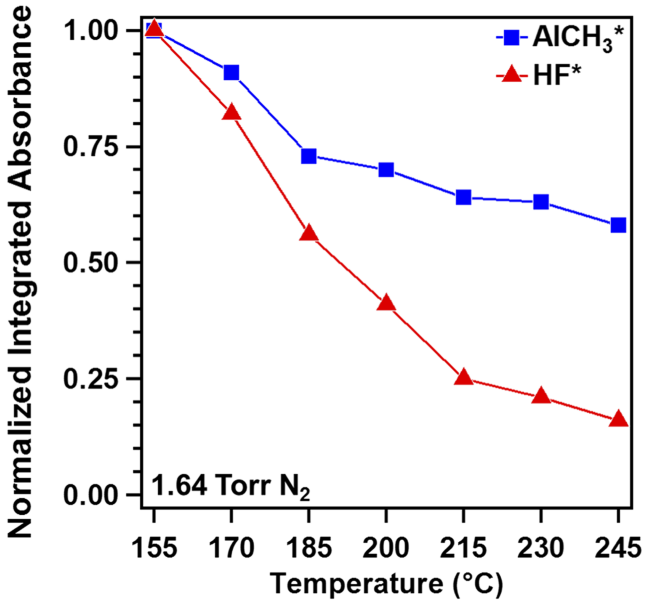

FIG. 4. Normalized integrated absorbance for the $AlCH_3^*$ and HF^* surface species versus temperature. The normalized integrated absorbance for the $AlCH_3^*$ species was measured by the C–H stretching vibrations between ~2800 and 3000 cm^{-1} after the TMA exposures. The normalized integrated absorbance for the HF^* species was measured by the H–F stretching vibrations between ~3000 and 3675 cm^{-1} after the HF exposures.

$AlF(CH_3)_2$ species that desorb from the surface to yield AlF_3 etching as shown in Figure 1(b).

The C–H stretching features in Figure 3 cannot distinguish between $AlF(CH_3)_2^*$ and $AlF_2(CH_3)^*$ species or $AlCH_3^*$ species on the Al_2O_3 surface. The $AlF(CH_3)_2^*$ and $AlF_2(CH_3)^*$ species or the $AlCH_3^*$ species on the Al_2O_3 surface are all expected to show asymmetric- and symmetric-CH_3 stretching modes between 2800 and 3000 cm^{-1}. FTIR spectra at lower frequencies can help to determine the identity of the adsorbed surface species. Figure 5 displays the FTIR difference spectra at lower frequencies between 500 and 950 cm^{-1} for consecutive TMA and HF exposures at 170, 200, and 245 °C, respectively.

Figure 5 shows the change in absorbance versus temperature for an absorbance feature that is centered at ~725 cm^{-1}. This feature is positive after the TMA exposures and negative after the HF exposures. This absorption feature is consistent with the Al–C stretching vibration of $AlF(CH_3)_2$ species.[22–24] Figure 5 reveals that this feature associated with $AlF(CH_3)_2$ decreases with temperature in agreement with Figure 1. An absorption feature is also monitored at ~900 cm^{-1}. This feature is negative after the TMA exposures and positive after the HF exposures. This feature may be consistent with intermolecular librations of HF^* species.[20]

C. Dependence of transition temperature on background pressure

Figure 6 shows the change in absorbance between 500 and 1200 cm^{-1} after 1, 5, and 10 TMA/HF cycles on an Al_2O_3 ALD film at various reaction temperatures. In contrast to the experimental results shown in Figure 2, these FTIR spectra were recorded with a constant flow of 50 sccm of UHP N_2 that resulted in a lower N_2 background pressure of 0.55 Torr in the

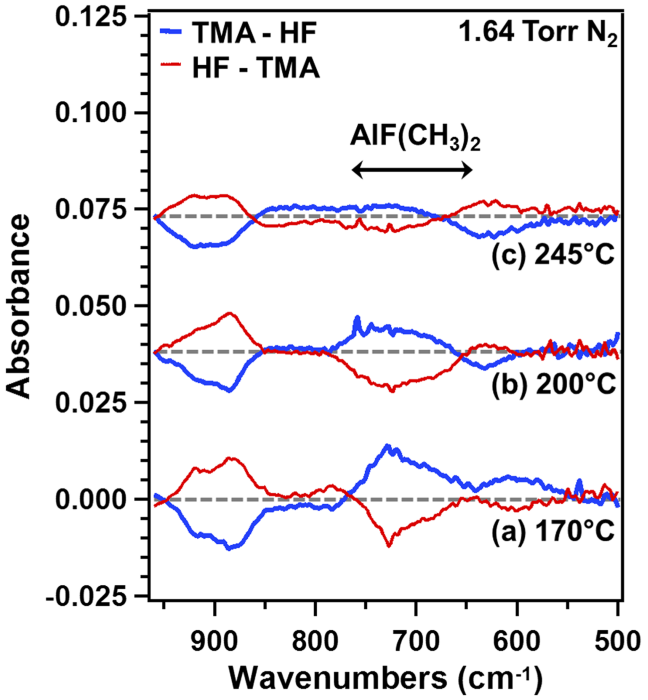

FIG. 5. Difference absorbance spectra from 500 to 900 cm^{-1} during TMA/HF exposures at 170, 200, and 245 °C. The difference spectra were recorded after HF and TMA exposures and were referenced using the spectra after the previous TMA and HF exposures, respectively.

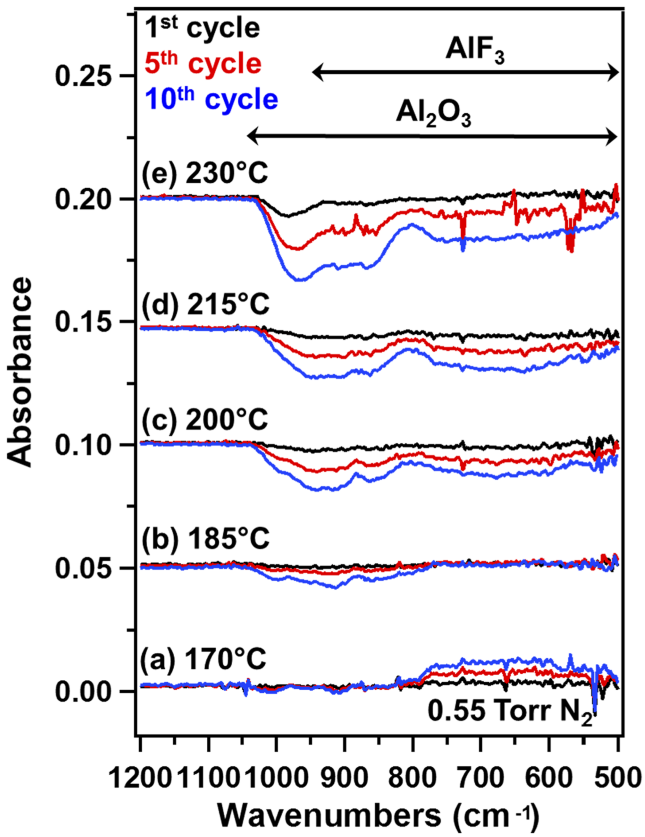

FIG. 6. Absorbance spectra showing the growth of Al–F stretching vibrations in AlF_3 or the removal of Al–O stretching vibrations in Al_2O_3 versus 1, 5, and 10 TMA/HF cycles at (a) 170, (b) 185, (c) 200, (d) 215, and (e) 230 °C. These FTIR spectra were recorded with an N_2 base pressure of 0.55 Torr after HF exposures and were referenced to the initial Al_2O_3 ALD-coated SiO_2 nanoparticles.

reactor. The spectra are again referenced to the Al_2O_3 ALD-coated SiO_2 nanoparticle substrate and are displaced from the origin for clarity in presentation.

Under these conditions with a lower N_2 background pressure of 0.55 Torr, the transition from the absorbance gain and AlF_3 film growth to absorbance loss and Al_2O_3 film removal occurs between 170 and 185 °C. This transition temperature is significantly lower than the transition temperature of 200 °C that was observed with a background pressure of 1.64 Torr for the results in Figure 2. These results indicate that the transition temperature between AlF_3 ALD and Al_2O_3 ALE is dependent on the background N_2 pressure in the reactor.

To explore this pressure dependence, experiments were performed at a variety of N_2 background pressures. Using UHP N_2 flow rates of 0, 50, 100, and 150 sccm defined N_2 background pressures of 0.03, 0.55, 1.05, and 1.64 Torr in the reactor, respectively. The absorbance changes were then measured after the TMA/HF reaction cycles at different reaction temperatures. Positive absorbance changes indicated AlF_3 ALD and negative absorbance changes indicated Al_2O_3 ALE. The transition between positive absorbance change and negative absorbance change defined the transition temperature.

Figure 7 shows the normalized absorbance changes per TMA/HF cycle measured over the entire spectral range between 500 and 1050 cm^{-1}. This range includes the Al–O stretching vibrations that absorb between 500 and 1050 cm^{-1} and the Al–F stretching vibrations that absorb between 500 and 900 cm^{-1}. The normalized absorbance changes are shown versus reaction temperature for N_2 background pressures of 0.03, 0.55, 1.05, and 1.64 Torr. Figure 7(a) shows the normalized absorbance change per cycle versus reaction temperature for a low background pressure of 0.03 Torr. A positive absorbance change indicating AlF_3 growth is observed at 155 °C. A small negative absorbance change indicating Al_2O_3 etching is observed at 170 °C. At progressively

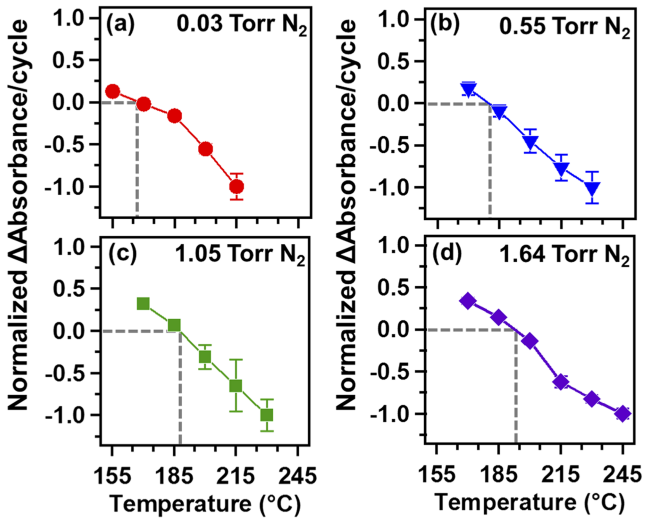

FIG. 7. Normalized change in absorbance per cycle between 500 and 1050 cm^{-1} versus temperature at N_2 gas pressures of (a) 0.03, (b) 0.55, (c) 1.05, and (d) 1.64 Torr.

higher reaction temperatures, the negative absorbance changes become larger, indicating higher amounts of Al_2O_3 etching.

Based on the results in Figure 7(a), the transition temperature between AlF_3 ALD and Al_2O_3 ALE occurs at ~168 °C. At this transition temperature, there is no net absorbance gain from Al–F stretching vibrations in AlF_3 and no net absorbance loss from Al–O stretching vibrations in Al_2O_3. The dashed lines indicate the transition temperature corresponding to no absorbance change per TMA/HF reaction cycle. $AlCH_3^*$ and HF^* surface species are still observed at the transition temperature after the TMA and HF exposures. However, these $AlCH_3^*$ and HF^* surface species do not lead to overall AlF_3 film growth or Al_2O_3 film removal. These surface species are added or lost versus TMA and HF exposures but do not result in a net gain or loss of material.

Figures 7(b)–7(d) display results for the transition temperature at higher N_2 background pressures of 0.55, 1.05, and 1.64 Torr, respectively. These results show that the transition temperature shifts to higher temperatures as the N_2 background pressure in the reactor increases. The transition temperatures are 181, 188, and 192 °C at N_2 background pressures of 0.55, 1.05, and 1.64 Torr, respectively.

A summary of all the transition temperatures versus N_2 background pressure is shown in Figure 8. The transition temperature rises rapidly with N_2 pressure from 0.03 to 1.64 Torr. The transition temperature then levels off for N_2 pressures >1.64 Torr. Figure 8 reveals that low temperatures and high pressures favor AlF_3 film growth by AlF_3 ALD. In contrast, high temperatures and low pressures favor Al_2O_3 film removal by Al_2O_3 ALE.

The transition between AlF_3 ALD and Al_2O_3 ALE can also be observed versus N_2 background pressure at a constant reaction temperature. Based on the transition temperature results shown in Figure 8, the transition from AlF_3 ALD to Al_2O_3 ALE would be expected to be observed as a function of reducing N_2 background pressure. Figure 9 shows the change in absorbance between 500 and 1200 cm^{-1} after 1, 5, and 10 TMA/HF cycles on an Al_2O_3 ALD film for progressively lower N_2 pressures at a constant temperature of 190 °C. The

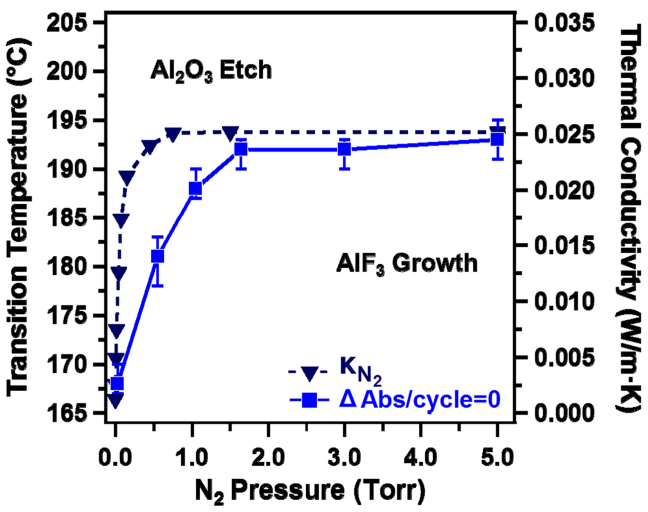

FIG. 8. Transition temperature for AlF_3 ALD to Al_2O_3 ALE versus N_2 pressure. The corresponding N_2 gas thermal conductivity versus N_2 pressure is shown for comparison.[25]

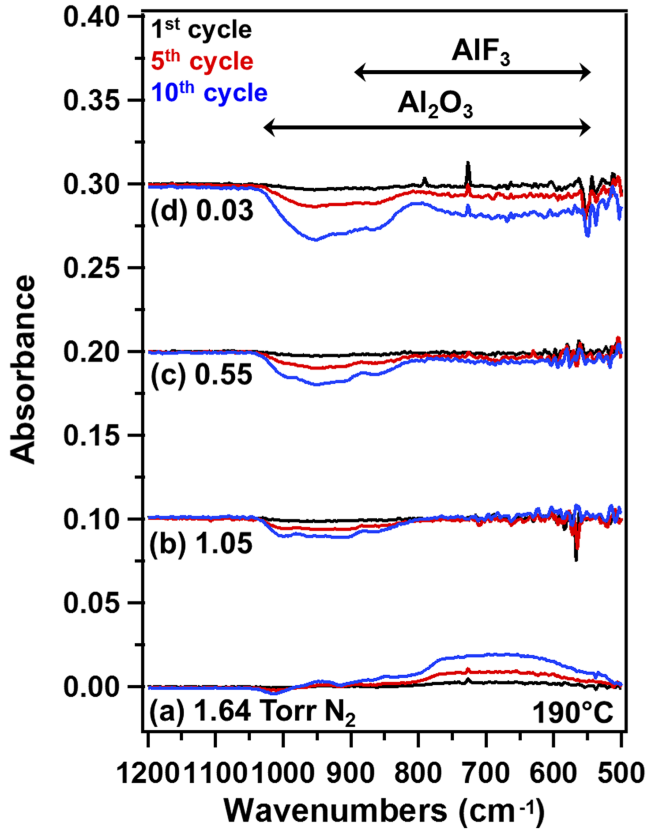

FIG. 9. Absorbance spectra showing the growth of Al–F stretching vibrations in AlF_3 or the removal of Al–O stretching vibrations in Al_2O_3 versus number of TMA/HF cycles at (a) 1.64, (b) 1.05, (c) 0.55, and (d) 0.03 Torr. These FTIR spectra were recorded at 190 °C after HF exposures and were referenced to the initial Al_2O_3 ALD-coated SiO_2 nanoparticles.

absorbance loss between 500 and 1050 cm^{-1} increases with reducing N_2 background pressures.

Figure 9 shows that more Al_2O_3 can be removed at lower pressures. At 190 °C, the transition between AlF_3 ALD and Al_2O_3 ALE occurs at a N_2 pressure between 1.64 Torr and 1.05 Torr. This result is in agreement with the transition temperatures versus N_2 background pressure displayed in Figure 8. The transition temperature of 190 °C in Figure 8 is consistent with a N_2 pressure of ~1.3 Torr.

D. Correlation between transition temperature and gas thermal conductivity

The results in Figure 8 are intriguing. The transition temperature versus N_2 pressure has a similar behavior to the N_2 gas thermal conductivity versus pressure. Gas thermal conductivity is dependent on the experimental configuration and the distance between the heat source and the heat sink. For various measurements, the N_2 gas thermal conductivity increases up to ~1 Torr and then is very constant at >1 Torr.[25,26] The N_2 gas thermal conductivity versus pressure obtained using the guarded hot plate method is displayed in Figure 8.[25]

The N_2 gas thermal conductivity can be understood from the kinetic theory of gases. The coefficient of thermal conductivity, κ, for a classical gas is given by

$$\kappa = 1/3\,\lambda\,\langle v\rangle\,C_v\,[A]\,, \qquad (1)$$

where [A] is the molar concentration, C_v is the heat capacity at constant volume, λ is the mean free path, and ⟨v⟩ is the mean speed.[27] At high pressures, where λ is inversely proportional to pressure and [A] is directly proportional to pressure, the thermal conductivity is independent of pressure. For N_2 gas, this region of constant gas thermal conductivity occurs at >1 Torr as shown in Figure 8. In this regime, the mean free path of the gas is much smaller than the dimension of the chamber. For example, at a N_2 pressure of 1 Torr and temperature of 190 °C, $\lambda \sim 8 \times 10^{-3}$ cm based on a N_2 collision diameter of 3.7×10^{-8} cm.[28]

As the pressure is reduced, the gas thermal conductivity decreases as the mean free path becomes longer and a smaller number of molecules can transfer heat. When the mean free path equals the dimension of the chamber, λ becomes constant and κ is proportional to P. The gas thermal conductivity then approaches zero as pressure is also reduced to zero. For N_2 gas, this regime of decreasing gas thermal conductivity occurs at <1 Torr as shown in Figure 8. This regime is the basis of pressure measurements using thermal conductivity (thermocouple) gauges.[29]

The N_2 gas thermal conductivity may affect the transition temperature because the N_2 gas thermal conductivity could influence the surface reactions during Al_2O_3 ALE. The fluorination of Al_2O_3 by HF is very exothermic. The fluorination reaction, $Al_2O_3 + 6HF \rightarrow 2AlF_3 + 3H_2O$, has a reaction enthalpy of $\Delta H = -102.75$ kcal/mol of Al_2O_3 at 200 °C.[30] In the high pressure region, the N_2 background pressure can cool the surface and dissipate the large reaction enthalpy. Little difference in cooling will result at pressures >1 Torr.

At lower pressures <1 Torr, the N_2 gas thermal conductivity decreases and the N_2 background gas will not as efficiently cool the surface. Consequently, the fluorination reaction will lead to higher temperature transients. The higher temperature transients may promote film etching by desorbing surface species that are essential for AlF_3 film growth. For example, the temperature transients may desorb the $AlCH_3^*$ and HF^* surface species. The loss of these surface species may shift the transition from AlF_3 ALD to Al_2O_3 ALE to lower temperatures.

To confirm that the gas thermal conductivity affects the transition temperature between AlF_3 ALD and Al_2O_3 ALE, similar experiments were performed using helium (He) as the background gas. Helium has a higher gas thermal conductivity than N_2 at higher pressures where the gas thermal conductivity is constant.[26,31] Helium also makes the transition from low gas thermal conductivity to higher gas thermal conductivity at a higher pressure range than N_2.[26,31] Consequently, similar experiments on the dependence of the transition temperature between AlF_3 ALD and Al_2O_3 ALE on the He background pressure may reveal different results than the correlation shown in Figure 8.

Figure 10 displays the AlF_3 ALD to Al_2O_3 ALE transition temperature versus gas pressure when He is used as the background gas during the TMA/HF exposures. The results are different than the results shown in Figure 8 for N_2 as the background gas. The transition temperature does not level out at higher He pressures. The He gas thermal conductivity derived by measuring heat flow across a helium gap versus pressure

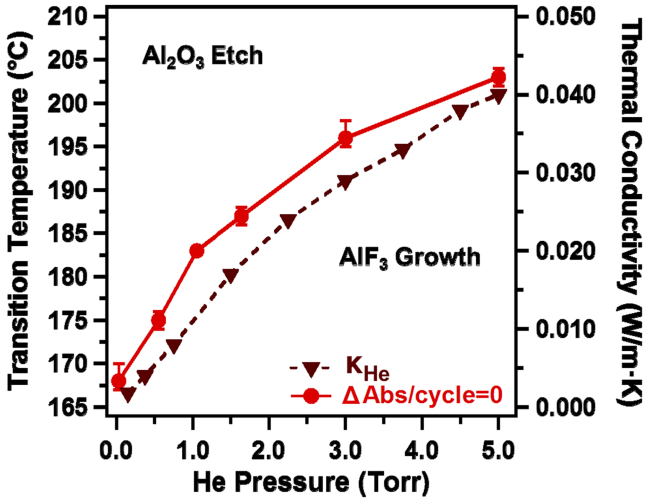

FIG. 10. Transition temperature for AlF_3 ALD to Al_2O_3 ALE versus He pressure. The corresponding He gas thermal conductivity versus He pressure is shown for comparison.[31]

is shown for comparison.[31] The He gas thermal conductivity also does not level out at higher He pressures. A constant gas thermal conductivity does not occur for He until a He pressure of ~75 Torr.[26,31]

There is a good correspondence in Figure 10 between the transition temperature and the He gas thermal conductivity. In this He pressure regime, the He gas thermal conductivity varies approximately linearly with the He pressure. The correlation in Figure 10 argues strongly that the He gas thermal conductivity determines the transition temperature between AlF_3 ALD and Al_2O_3 ALE. Like the interpretation of the results in Figure 8, the He gas thermal conductivity affects the transition temperature if the higher temperature transients corresponding with lower He gas thermal conductivities are able to desorb the $AlCH_3^*$ and HF^* surface species that are responsible for the AlF_3 growth or Al_2O_3 etching.

Figure 4 revealed the thermal stability of the $AlCH_3^*$ and HF^* surface species at an N_2 background gas pressure of 1.64 Torr. Similar experiments examined the absorbances of the infrared features associated with the $AlCH_3^*$ and HF^* surface species during TMA/HF reaction cycles versus temperature at constant background He pressure and versus He pressure at constant temperature. These experiments can access whether the thermal stability of the $AlCH_3^*$ and HF^* surface species is dependent on the nature of the background gas.

Figure 11(a) shows the normalized integrated absorbance of the vibrational features located between 3000 and 3675 cm^{-1} for the HF^* surface species and between 2800 and 3000 cm^{-1} for the $AlCH_3^*$ surface species versus temperature when the background He pressure was held constant at 3.0 Torr. The normalized integrated absorbances for the $AlCH_3^*$ and HF^* surface species decrease as the temperature is increased from 170 °C to 230 °C. The absorbances for the $AlCH_3^*$ and HF^* surface species show reductions of 33% and 70%, respectively, over this temperature range.

The results in Figure 11(a) indicate that the HF^* surface species is much more temperature-dependent than the $AlCH_3^*$ surface species. These results are consistent with the previous

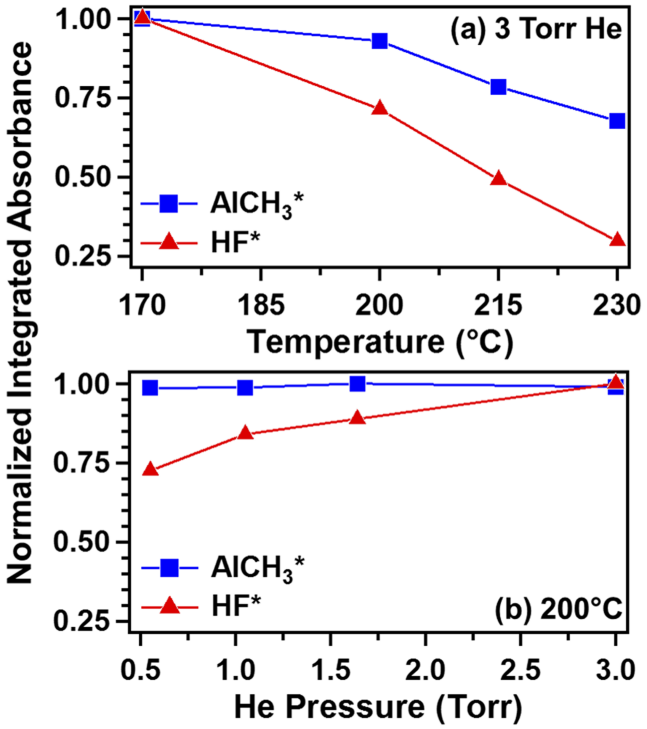

FIG. 11. (a) Normalized integrated absorbance for the $AlCH_3^*$ and HF^* surface species versus temperature at He gas pressure of 3 Torr. (b) Normalized integrated absorbance for the $AlCH_3^*$ and HF^* surface species versus He pressure at a temperature of 200 °C. The normalized integrated absorbances were measured using the same procedure as employed in Figure 4.

results for the stability of the $AlCH_3^*$ and HF^* surface species in a N_2 background pressure of 1.64 Torr shown in Figure 4. The similarity of the results in Figures 4 and 11 indicates that the nature of the gas does not influence the thermal stability of the $AlCH_3^*$ and HF^* species. The higher temperature transients at lower gas thermal conductivity will lead to the loss of both $AlCH_3^*$ and HF^* surface species.

Figure 11(b) shows the normalized integrated absorbance of the $AlCH_3^*$ and HF^* surface species versus He pressure when the temperature was held constant at 200 °C. Little change in the integrated absorbance of the $AlCH_3^*$ species was observed for He pressures from 0.5 to 3.0 Torr. In contrast, the integrated absorbance of the HF^* surface species increases at higher He pressure. The integrated absorbance of the HF^* surface species is about 25% higher at 3.0 Torr than at 0.5 Torr. The results in Figure 11(b) confirm that the HF^* surface species is more susceptible to temperature changes than the $AlCH_3^*$ surface species.

E. Temperature transients for nanoparticles and silicon wafers

These FTIR experiments were conducted on high surface area SiO_2 nanoparticles. The temperature transients resulting from the fluorination reactions may be much higher on SiO_2 nanoparticles compared with the temperature transients on bulk substrates because bulk substrates have a much larger thermal bath. In addition, the temperature transients on the SiO_2 nanoparticles may be much longer than the temperature transients on bulk substrates because the heat transfer will have a much more tortuous path in a sample of SiO_2 nanoparticles. Consequently, the transition temperature between AlF_3 ALD and Al_2O_3 ALE may be very different between nanoparticles and bulk substrates.

The temperature transient that would occur on an isolated Al_2O_3 ALD-coated SiO_2 nanoparticle can be estimated based on the fluorination thermochemistry, the amount of fluorination, and the mass and heat capacity of a SiO_2 nanoparticle. As mentioned earlier, the fluorination reaction, $Al_2O_3 + 6HF \rightarrow 2AlF_3 + 3H_2O$, has a reaction enthalpy of $\Delta H = -102.75$ kcal/mol of Al_2O_3 at 200 °C.[30] The total amount of Al_2O_3 converted to AlF_3 during each HF exposure can be approximated based on previous quartz crystal microbalance (QCM) investigations.[8] These QCM studies have shown that the mass changes are consistent with the fluorination of an Al_2O_3 layer with a thickness of 1.7 Å to yield an AlF_3 layer with a thickness of 3.0 Å.[8]

The initial Al_2O_3 ALD-coated SiO_2 nanoparticle has an Al_2O_3 thickness of 10 Å on the SiO_2 nanoparticles with a 20 nm diameter. The fluorination of an Al_2O_3 layer with a thickness of 1.7 Å to yield an AlF_3 layer with a thickness of 3.0 Å would result in 2.55×10^5 Å^3 of Al_2O_3 converted to AlF_3 on the SiO_2 nanoparticle during the HF exposure. Based on the density of 3.0 g/cm^3 for Al_2O_3 ALD films grown at 170 °C, the mass of Al_2O_3 converted to AlF_3 is 7.64×10^{-19} g. This mass of Al_2O_3 is equivalent to 7.49×10^{-21} mol of Al_2O_3. The heat produced by fluorinating this quantity of Al_2O_3 is 7.69×10^{-16} cal or 3.22×10^{-15} J.

In the limit that all of this heat is deposited in the isolated SiO_2 nanoparticle, the temperature transient can be determined based on the mass of the SiO_2 nanoparticle and the specific heat capacity for SiO_2. Using a density of 2.2 g/cm^3, the mass of a SiO_2 nanoparticle with a diameter of 20 nm is 9.22×10^{-18} g. If all the heat is deposited in the SiO_2 nanoparticle, then the temperature transient in the SiO_2 nanoparticle is $\Delta T = 497$ K using a specific heat capacity for SiO_2 of 703 (J/kg)/K. This calculation reveals that the reaction enthalpy of fluorination can lead to large temperature changes in the isolated SiO_2 nanoparticle.

In the actual experiment, the heat from the fluorination reaction can diffuse to the tungsten grid and then to the sample holder. The heat from the fluorination reaction can also dissipate to the surrounding background gas depending on the gas thermal conductivity. However, the model calculation assuming an isolated SiO_2 nanoparticle reveals that the fluorination reaction enthalpy can easily produce significant temperature transients in the SiO_2 nanoparticle that could affect the surface species on the SiO_2 nanoparticle and influence the etching reaction.

Compared with SiO_2 nanoparticles, the temperature transients will be much less for the fluorination reaction during Al_2O_3 ALE of Al_2O_3 films on substrates such as silicon wafers. These substrates have a much larger thermal bath to dissipate the heat of fluorination. Assuming a 1 cm^2 silicon wafer with a thickness of 250 μm as the thermal bath, the fluorination of a 1 cm^2 Al_2O_3 layer on the silicon wafer with a thickness of 1.7 Å to yield an AlF_3 layer with a thickness of 3.0 Å would result in 1.7×10^{-8} cm^3 of Al_2O_3 converted to AlF_3 during the HF exposure. The mass of this volume of Al_2O_3 is

5.1×10^{-8} g. This mass of Al_2O_3 is equivalent to 5.00×10^{-10} moles of Al_2O_3. The heat produced by fluorinating this quantity of Al_2O_3 is 5.14×10^{-5} cal or 2.15×10^{-4} J.

In the limit that all of this heat is deposited in the underlying silicon wafer, the temperature transient can be determined based on the mass of the silicon wafer and the specific heat capacity for silicon. Using a density of 2.2 g/cm^3, the mass of a 1 cm^2 silicon wafer with a thickness of 250 μm is 5.82×10^{-2} g. If all the heat of the fluorination reaction is deposited in the silicon wafer, then the temperature transient in the silicon wafer is predicted to be $\Delta T = 5 \times 10^{-3}$ K. This prediction used a specific heat capacity for silicon of 712 (J/kg)/K.

These calculations illustrate that the large thermal bath provided by bulk substrates will result in very small temperature transients during fluorination. These small transients will lead to an ALD to ALE transition temperature that is independent of background gas pressure. In contrast, the measured dependence of the transition temperature on pressure in this study is the result of using SiO_2 nanoparticles to monitor the ALD to ALE transition temperature. Dependence of the ALD to ALE transition temperature on gas pressure should be expected for other nanoparticle substrates.

IV. CONCLUSIONS

There is a rivalry between Al_2O_3 ALE and AlF_3 ALD when using TMA and HF as the reactants. This competition between removal and growth processes was studied using *in situ* FTIR vibrational spectroscopy measurements on Al_2O_3 ALD-coated SiO_2 nanoparticles. The signatures of Al_2O_3 ALE or AlF_3 ALD were the absorbance loss of the Al–O stretching vibrations during Al_2O_3 ALE and the absorbance gain of the Al–F stretching vibrations during AlF_3 ALD. The transition from AlF_3 ALD to Al_2O_3 ALE occurred versus reaction temperature. The transition temperature was also influenced by the N_2 or He background gas pressure.

The FTIR spectra observed $AlCH_3^*$ and HF^* species on the surface after the TMA reactant and HF exposures. The loss of $AlCH_3^*$ and HF^* species at higher temperatures is believed to be responsible for the transition between AlF_3 ALD and Al_2O_3 ALE. At low temperature, TMA can react with the high coverage of HF^* species and HF can react with the high coverage of $AlCH_3^*$ species and produce AlF_3 ALD. At higher temperatures, the low coverage of HF^* species enables TMA to react with the AlF_3 surface layer in a ligand-exchange reaction to produce volatile $AlF(CH_3)_2$ reaction products. The low coverage of $AlCH_3^*$ species also enable HF to convert the Al_2O_3 surface to an AlF_3 surface layer.

The transition between AlF_3 ALD at lower temperature and Al_2O_3 ALE at higher temperature was defined by the transition temperature. Higher transition temperatures were observed using larger N_2 or He background gas pressures. The correlation between the transition temperature and the N_2 or He background gas pressures was linked to changes of the N_2 or He gas thermal conductivity versus pressure. This correlation indicates that heat dissipation by gas thermal conduction affects the temperature rise during the fluorination reaction. Higher temperature transients are able to desorb surface species that enable Al_2O_3 etching. The higher gas thermal conductivities can more effectively cool the SiO_2 nanoparticles and reduce the size of the temperature transients.

The rivalry between Al_2O_3 ALE and AlF_3 ALD using TMA and HF as the reactants illustrates the interplay between etching and growth. Substrate temperature plays an important role in determining the coverage of the $AlCH_3^*$ and HF^* surface species that dictate whether conditions favor Al_2O_3 ALE and AlF_3 ALD. Background gas pressure also is important in determining the transition temperature for nanoparticle substrates when large temperature transients can result from the fluorination reaction.

ACKNOWLEDGMENTS

This research was funded by the National Science Foundation (Grant Nos. CHE-1306131 and CHE-1609554).

[1] S. M. George, "Atomic layer deposition: An overview," Chem. Rev. **110**, 111–131 (2010).
[2] K. J. Kanarik, T. Lill, E. A. Hudson, S. Sriraman, S. Tan, J. Marks, V. Vahedi, and R. A. Gottscho, "Overview of atomic layer etching in the semiconductor industry," J. Vac. Sci. Technol., A **33**, 020802 (2015).
[3] C. T. Carver, J. J. Plombon, P. E. Romero, S. Suri, T. A. Tronic, and R. B. Turkot, "Atomic layer etching: An industry perspective," ECS J. Solid State Sci. Technol. **4**, N5005–N5009 (2015).
[4] V. Miikkulainen, M. Leskela, M. Ritala, and R. L. Puurunen, "Crystallinity of inorganic films grown by atomic layer deposition: Overview and general trends," J. Appl. Phys. **113**, 021301 (2013).
[5] Y. Lee, J. W. DuMont, and S. M. George, "Mechanism of thermal Al_2O_3 atomic layer etching using sequential reactions with $Sn(acac)_2$ and HF," Chem. Mater. **27**, 3648–3657 (2015).
[6] Y. Lee, J. W. DuMont, and S. M. George, "Atomic layer etching of AlF_3 using sequential, self-limiting thermal reactions with $Sn(acac)_2$ and hydrogen fluoride," J. Phys. Chem. C **119**, 25385–25393 (2015).
[7] Y. Lee, J. W. DuMont, and S. M. George, "Atomic layer etching of HfO_2 using sequential, self-limiting thermal reactions with $Sn(acac)_2$ and HF," ECS J. Solid State Sci. Technol. **4**, N5013–N5022 (2015).
[8] Y. Lee, J. W. DuMont, and S. M. George, "Trimethylaluminum as the metal precursor for the atomic layer etching of Al_2O_3 using sequential, self-limiting thermal reactions," Chem. Mater. **28**, 2994–3003 (2016).
[9] Y. Lee and S. M. George, "Atomic layer etching of Al_2O_3 using sequential, self-limiting thermal reactions with $Sn(acac)_2$ and hydrogen fluoride," ACS Nano **9**, 2061–2070 (2015).
[10] N. R. Johnson, H. Sun, K. Sharma, and S. M. George, "Thermal atomic layer etching of crystalline aluminum nitride using sequential, self-limiting HF and $Sn(acac)_2$ reactions and enhancement by H_2 and Ar plasmas," J. Vac. Sci. Technol., A **34**, 050603 (2016).
[11] S. M. George and Y. Lee, "Prospects for thermal atomic layer etching using sequential, self-limiting fluorination and ligand-exchange reactions," ACS Nano **10**, 4889–4894 (2016).
[12] Y. Lee, H. Sun, M. J. Young, and S. M. George, "Atomic layer deposition of metal fluorides using HF–pyridine as the fluorine precursor," Chem. Mater. **28**, 2022–2032 (2016).
[13] R. L. Puurunen, "Surface chemistry of atomic layer deposition: A case study for the trimethylaluminum/water process," J. Appl. Phys. **97**, 121301 (2005).
[14] Y. Lee, J. W. DuMont, A. S. Cavanagh, and S. M. George, "Atomic layer deposition of AlF_3 using trimethylaluminum and hydrogen fluoride," J. Phys. Chem. C **119**, 14185–14194 (2015).
[15] J. W. DuMont and S. M. George, "Pyrolysis of alucone molecular layer deposition films studied using *in situ* transmission Fourier transform infrared spectroscopy," J. Phys. Chem. C **119**, 14603–14612 (2015).
[16] T. H. Ballinger, J. C. S. Wong, and J. T. Yates, "Transmission infrared-spectroscopy of high area solid surfaces—A useful method for sample preparation," Langmuir **8**, 1676–1678 (1992).
[17] J. D. Ferguson, A. W. Weimer, and S. M. George, "Atomic layer deposition of ultrathin and conformal Al_2O_3 films on BN particles," Thin Solid Films **371**, 95–104 (2000).

[18]W. Heitmann, "Vacuum evaporated films of aluminum fluoride," Thin Solid Films **5**, 61–67 (1970).
[19]U. Gross, S. Rudiger, E. Kemnitz, K. W. Brzezinka, S. Mukhopadhyay, C. Bailey, A. Wander, and N. Harrison, "Vibrational analysis study of aluminum trifluoride phases," J. Phys. Chem. A **111**, 5813–5819 (2007).
[20]P. Ayotte, M. Hebert, and P. Marchand, "Why is hydrofluoric acid a weak acid?," J. Chem. Phys. **123**, 184501 (2005).
[21]A. C. Dillon, A. W. Ott, J. D. Way, and S. M. George, "Surface chemistry of Al_2O_3 deposition using $Al(CH_3)_3$ and H_2O in a binary reaction sequence," Surf. Sci. **322**, 230–242 (1995).
[22]A. P. Gray, "Infrared spectra of trimethyl aluminum, dimethyl aluminum chloride, methyl aluminum dichloride, methyl titanium trichloride, dimethyl titanium dichloride, and some deuterium derivatives," Can. J. Chem. **41**, 1511–1521 (1963).
[23]M. P. Groenewege, "An I. R. spectroscopic study of the components of the Ziegler catalyst system $TiCl_4$ + $Al(CH_3)_2Cl$," Z. Phys. Chem. **18**, 147–162 (1958).
[24]J. Weidlein and V. Krieg, "Vibrational spectra of dimethyl and diethyl aluminum fluoride," J. Organomet. Chem. **11**, 9–16 (1968).
[25]L. F. Su, L. Miao, S. Tanemura, and G. Xu, "Low-cost and fast synthesis of nanoporous silica cryogels for thermal insulation applications," Sci. Technol. Adv. Mater. **13**, 035003 (2012).
[26]D. Ganta, E. B. Dale, J. P. Rezac, and A. T. Rosenberger, "Optical method for measuring thermal accommodation coefficients using a whispering-gallery microresonator," J. Chem. Phys. **135**, 084313 (2011).
[27]P. W. Atkins, *Physical Chemistry* (Oxford University Press, Oxford, 1990).
[28]A. Roth, *Vacuum Technology* (Elsevier Science B.V., Amsterdam, 1990).
[29]R. E. Ellefson and A. P. Miiller, "Recommended practice for calibrating vacuum gauges of the thermal conductivity type," J. Vac. Sci. Technol., A **18**, 2568–2577 (2000).
[30]HSC Chemistry, Version 5.1, Outokumpu Research Oy, Pori, Finland.
[31]A. Lucianetti, D. Albach, and J. C. Chanteloup, "Active-mirror-laser-amplifier thermal management with tunable helium pressure at cryogenic temperatures," Opt. Express **19**, 12766–12780 (2011).